Advanced Biomedical Engineering
8: 63–77, 2019.

Original Paper

DOI:10.14326/abe.8.63

Finite Element Predictions of Sutured and Coupled Microarterial Anastomoses

Richard AJ Wain,[*, **, ***, #] Nicolas J Gaskell,[*] Andrew M Fsadni,[*]
Jonathan Francis,[*] Justin PM Whitty[*]

Abstract Simulation using computational methods is well-established for investigating mechanical and haemodynamic properties of blood vessels, however few groups have applied this technology to microvascular anastomoses. This study, for the first time, employs analytic and numeric models of sutured and coupled microarterial anastomoses to evaluate the elastic and failure properties of these techniques in realistic geometries using measured arterial waveforms. Computational geometries were created of pristine microvessels and microarterial anastomoses, performed using sutures and a coupling device. Vessel wall displacement, stress, and strain distributions were predicted for each anastomotic technique using finite element analysis (FEA) software in both static and transient simulations. This study focussed on mechanical properties of the anastomosis immediately after surgery, as failure is most likely in the early post-operative period. Comparisons were also drawn between stress distributions seen in analogous non-compliant simulations. The maximum principal strain in a sutured anastomosis was found to be 84% greater than in a pristine vessel, whereas a mechanically coupled anastomosis reduced arterial strain predictions by approximately 55%. Stress distributions in the sutured anastomoses simulated here differed to those in reported literature. This result is attributed to the use of bonded connections in existing studies, to represent healed surgical sites. This has been confirmed by our study using FEA, and we believe this boundary condition significantly alters the stress distribution, and is less representative of the clinical picture following surgery. We have demonstrated that the inertial effects due to motion of the vessel during pulsatile flow are minimal, since the differences between the transient and static strain calculations range from around 0.6–7% dependent on the geometry. This implies that static structural analyses are likely sufficient to predict anastomotic strains in these simulations. Furthermore, approximations of the shear strain rate (SSR) were calculated and compared to analogous rigid-walled simulations, revealing that wall compliance had little influence on their overall magnitude. It is important to highlight, however, that SSR variations here are taken in isolation, and that changing pressure gradients are likely to produce much greater variation in vessel wall strain values than the influence of fluid flow alone. Hence, a formal fluid-structure interaction (FSI) study would be necessary to ascertain the true relationship.

Keywords: Finite Element Analysis (FEA), Finite Element Method (FEM), anastomosis, microvascular, microarterial, suture, coupler.

Adv Biomed Eng. **8**: pp. 63–77, 2019.

1. Introduction

Microvascular anastomoses are performed when blood vessels of approximately 1–3 mm diameter are surgically joined together. One of the most common indications for this is autologous free-tissue transfer for reconstruction of oncological or traumatic defects. In these cases, both arteries and veins must be detached completely from their donor site and anastomosed with local recipient vessels, an intricate procedure requiring intraoperative microscopy. Whilst many techniques have been proposed for anastomosing these structures [1], suturing remains the mainstay for arteries; and both sutured and mechanical coupling are routine practice for veins [2–4].

Sutured anastomoses are hand sewn using fine stitches made from monofilament nylon or polypropylene of approximately 0.03–0.04 mm diameter [5]. An

Received on September 3, 2018; revised on December 18, 2018; accepted on January 6, 2019.

[*] John Tyndall Institute, School of Engineering, University of Central Lancashire, Preston, UK.

[**] School of Medicine and Dentistry, University of Central Lancashire, Preston, UK.

[***] Department of Plastic & Reconstructive Surgery, Royal Preston Hospital, Lancashire Teaching Hospitals NHS Foundation Trust, Preston, UK.

[#] Preston PR1 2HE, UK.
E-mail: richwain@doctors.org.uk

average of 8 individual sutures are placed around the circumference of a typical calibre (2.5 mm) artery and, although a range of suturing techniques exist, outcomes remain largely unchanged provided good microsurgical practice is adhered to [6].

Coupled anastomoses are also performed by hand, but are assisted with the use of a mechanical delivery system whereby interlocking ring-pin devices are placed over the vessel ends and then pressed together. The ring-pin concept was first proposed in 1900 by Payr [7] and has taken a range of development steps [8, 9] to become the commercially available Microvascular Anastomotic Coupler (MAC) device used today [10]. Historically, most free-flap failures occurred due to thrombus in venous anastomoses, however refinement and routine use of the MAC system has reduced failures to ~0.6% in some centres [3, 11]. The coupler is licensed for use in arteries but this is not common practice due to technical difficulty, despite a small number of studies reporting successful outcomes [12–15].

Free-tissue transfer is well-established and provides high success rates in the majority of cases. Inherent failure rates are approximately 5–10% in emergency, and 2–3% in routine, procedures [16–20]. These failures are predominantly due to formation of thrombus at the anastomosis, and can lead to failure of the entire reconstructive procedure.

Factors precipitating thrombosis in these procedures are numerous [21, 22], however one such factor is the activation and deposition of platelets at the anastomotic site [22–26]. It is well known that platelets become activated when exposed to high shear strain rates (SSR), and that this is exacerbated by exposure to subendothelium and injured vessel walls [27–29]. Measurement of these aspects of flow is technically challenging *in vivo* and as such, approximations are often made through the use of computational simulation [30].

1.1 Computational simulation of arteries

Work by this group has explored the SSR profiles of a range of microarterial anastomoses in idealized and realistic geometries, in both steady-state and transient flows [31–35], using the computational fluid dynamics (CFD) software ANSYS-CFX. Whilst these simulations were designed to represent clinical practice closely, they were all performed using rigid vessels which, although may be a reasonable assumption [30], is not the case physiologically.

In a similar way to SSR, wall shear stress (WSS) has been simulated in arterial flows by a number of groups [36, 37]. Interest in WSS was initiated after its link to vessel wall thickening, or hyperplasia, was made as intimal hyperplasia is thought to contribute to long-term failure of vascular grafts [38, 39]. It has been proposed that compliance mismatch between vascular grafts and their recipient artery is a principal cause of hyperplasia and subsequent failure, as matching the compliance results in improved patency [40]. This is more pronounced in end-to-side rather than end-to-end anastomoses, with abnormal haemodynamics at the suture line being a main cause [41–44].

Although a large number of studies have made stress predictions in large to medium sized arteries using computational simulations of flow [45–49], use of the finite element method (FEM) to model this behaviour in microvessels, particularly at anastomoses, is restricted to a just a few. Al-Sukhun *et al*. performed two finite element analysis (FEA) studies specifically evaluating stress distributions in microanastomoses [50, 51]. This group concluded that size discrepancy adversely influenced blood flow and deformation [50] and that principal stresses were much less at the anastomotic site in compliant rather than rigid-walled vessels [51]. Whilst these findings are helpful, both studies used pristine ducts to represent vessels (*i.e.* not accounting for the positioning or presence of sutures, an essential aspect of the surgical procedure). There are a small number of groups who have explored sutures using FEA, with the work of Ballyk *et al.* [40] being the earliest. Here, simulations of peripheral artery bypass procedures were performed to evaluate compliance mismatch between the artery and graft, and the influence of suture line stresses on potential for intimal hyperplasia. Sutures were approximated as spot-welds for simulation purposes. It was concluded that compliance mismatch was less pronounced in end-to end anastomoses, but that high suture line stresses might be a stimulus for vessel wall thickening in all vessel repairs [40]. These findings are largely supported by the work of Perktold *et al*. [48] who simulated sutures as weak springs in some cases, but also incorporated the mechanical properties of suture material in other simulations. An analogous study was performed by Liu *et al*. [52] whereby the stress distributions at the wall were evaluated when surgical knots were tied in robot-assisted anastomoses. That study demonstrated upper limits of tension across an anastomosis to prevent vessel wall injury, and represents one of the few studies using FEA to simulate suture-line stresses [52]. One recent study used FEA to evaluate the design concept of a coupling device [53], although this was performed in isolation and in a device which is now obsolete.

In each of these cases the representative domain of interest (*e.g.* artery, vein, anastomotic site, *etc.*) is divided in to a number of elements which are connected at nodes. Each element, being finite in size, adheres to the renowned equation [54–56]:

$$k_i = h \iint_A \overrightarrow{B}[\boldsymbol{D}]\overrightarrow{B}^T dA \quad (1)$$

where k_i is the so-called element stiffness matrix, $\overrightarrow{B}$ ($\nabla\overrightarrow{N}$, equation (9)) is the gradient of the shape function vector and h is the shell thickness. Whilst [$\boldsymbol{D}$] is the elastic coupling, which throughout the work herein takes the form of the shell compliance tensor [57]; this being a function of the modulus of elasticity and the Poisson's ratio [58]. The elementary principles of FEA represent an extension of Courant's method [59] consisting of minimizing functionals using variational calculus. Each of these individual element matrices are then assembled together in order to provide for solution of underlying partial differential equations (PDEs), so that conditions of equilibrium and compatibility are satisfied.

1.2 Motivation and scope

There is a growing body of research related to the prediction of flow properties in microanastomoses [32, 33, 35, 60, 61]. The focus of these studies being evaluation of shear stresses and strain rates to provide inference regarding the propensity for thrombosis formation, and hence anastomotic failure. The majority of these studies model blood vessels as structures with non-compliant *i.e.* rigid walls, an assumption justified to an extent by Steinman [30]. However, as blood vessels are not rigid under normal physiological conditions, a natural progression of such work is to relax this assumption, this being the principal motivation for the study described herein.

In this paper we employ analytic and numeric (FEA) models of sutured and coupled microarterial anastomoses to evaluate the elastic and failure properties of these techniques. Furthermore, verification is provided of the elastic response at anastomotic sites when subjected to static and physiological transient pressure changes. Derived quantities of stresses and strains, along with simulation of the elastic responses of these vessels, are used to infer failure criteria under appropriate boundary conditions. Finally, we draw comparisons between the stress distributions seen in analogous non-compliant FEA and CFD simulations.

2. Methods

In this section geometric and material properties used to perform these simulations are described, along with their justification compared to existing work. Details of analytic routines *i.e.* thick-wall cylinder theory static analysis and sinusoidal dynamic simulations, are provided, in addition to application of a physiological arterial pulse. Furthermore, specifics of the FEA simulations including creation of the sutured and coupled arterial models, and their meshing routines, are provided.

2.1 Material and geometric properties

In order to simulate the mechanical properties of vessel walls, some key parameter values are needed and specific assumptions must be made. Burton [62], concluded that the average elastic modulus (E) of arterial walls was 455 kPa with the Poisson's ratio (ν) being 0.28. Works from Al-Sukhun *et al*. [50, 51], Abbot *et al.* [63] and Kahveci [64] have employed these values. Chandran *et al*. [65] used a Poisson's ratio of 0.49 for arteries in their work, and values of 0.5 have been employed elsewhere [66]. Ratios ranging from 0.29–0.71 have been reported in experimental studies on canine vessels demonstrating anisotropy [67], with inconsistencies in measured Poisson's ratios being highlighted in work by Skacel [68]. However, given that simulations performed herein are akin to those by Al-Sukhun *et al*. [50, 51] and Kahveci [64], values of 455 kPa and 0.28 for the modulus of elasticity (E) and Poisson's ratio (ν) respectively, were entered as *Engineering Data* within ANSYS Workbench [69, 70]. The density of the arterial walls was approximated to $1000\,\mathrm{kgm}^{-3}$ in keeping with the same studies [50, 51, 64, 65].

All vessels were modelled as cylindrical ducts of british 2.5 mm diameter in the same way as for previous studies [33, 35]. Here, mean values of vessel diameter were obtained using anonymized Doppler ultrasonographybritish[1] scans of deep inferior epigastric arteries (DIEA) during preoperative assessment for breast reconstruction surgery.

2.2 Analytic

Whilst anatomically blood vessel walls are composed of several layers, each with individual mechanical and structural properties, the extent to which these are significant depends on the nature of the problem under investigation. As for a range of previous works [40, 48, 50, 51, 64, 65], the vessel walls in this study were assumed isotropic, homogeneous, and to adhere to thick-wall cylinder theory. In this section, analytic expressions for each of the principal strain fields are derived from Lamnd Clapeyron thick-wall cylinder theory. Additionally, Fast Fourier Transform (FFT) techniques are used to obtain analytic representations of empirical data. Finally, a rudimentary method is used to calculate approximations of Shear Strain Rate (SSR) at the vessel wall to enable comparison with previous CFD studies.

2.2.1 Thick-wall cylinders

The radius to thickness ratio of the arteries in this study was greater than ten (*i.e.* $\bar{R}/t \geq 10$, with $\bar{R}$ being the aver-

[1] Phillips iU22 ultrasound scanner and L9-3 probe (Philips Healthcare, 5680 DA Best, The Netherlands)

age *characteristic* radius and t being the wall thickness), as such application of Lamlapeyron thick-wall cylinder theory is appropriate. The basic underlying assumption being that these vessels consist of a series of thin-walled cylinders exerting pressure unto each other, which is the case anatomically. Given that details of the intrinsic stress-strain relationship is not clearly defined for what, in reality is a composite series of thin walls, we assume that maximum principal strain failure criterion is appropriate here. Furthermore, the Lamlapeyron cylinder theory, together with the Poisson's effect renders:

$$\begin{aligned}\varepsilon_\theta =& \frac{1}{E}\left(\frac{R_i^2}{R_o^2-R_i^2}\left\{1+\frac{R_o^2}{r^2}\right\}p(t)\right)\\ &-\frac{\nu}{E}\left(\frac{R_i^2}{R_o^2-R_i^2}\left\{1-\frac{R_o^2}{r^2}\right\}p(t)\right)\\ &-\frac{\nu}{E}\left(\frac{R_i^2}{R_o^2-R_i^2}\frac{p(t)}{10}\right),\end{aligned}$$

where ε_θ is principal strain, R_i and R_o are internal and external radii of the arteries respectively, ν and E are the arterial Poisson's ratio and elastic modulus respectively, r is the spatial coordinate, and $p(t)$ is the internal pressure. The factor to 10 in the final term being included to simulate the effects of the rest of the cardiovascular system. That is, in all of the simulations that follow, the end pressure was set to 10% of the systolic pressure (1.6 kPa) [71]. Each of the expressions in parenthesis being the first (hoop), the second (radial) and third (longitudinal) principal stresses respectively, whence:

$$\begin{aligned}\varepsilon_1=&\varepsilon_\theta\\ =&\frac{R_i^2}{R_o^2-R_i^2}\left\{\frac{1-\nu}{E}+\left\{\frac{1+\nu}{E}\right\}\frac{R_o^2}{r^2}-\frac{\nu}{10E}\right\}p(t),\end{aligned} \tag{2}$$

similarly, the second principal strain can be found, thus:

$$\begin{aligned}\varepsilon_2=&\varepsilon_r\\ =&\frac{R_i^2}{R_o^2-R_i^2}\left\{\frac{1-\nu}{E}-\left\{\frac{1+\nu}{E}\right\}\frac{R_o^2}{r^2}-\frac{\nu}{10E}\right\}p(t).\end{aligned} \tag{3}$$

Furthermore, the third principal (longitudinal) strain can be shown to be constant:

$$\begin{aligned}\varepsilon_3 =& \left(\frac{R_i^2}{R_o^2-R_i^2}\right)\left\{\frac{\nu}{10E}p(t)-\frac{\nu}{E}\left(\left\{1+\frac{R_o^2}{r^2}\right\}p(t)\right)\right.\\ &\left.-\frac{\nu}{E}\left(\left\{1-\frac{R_o^2}{r^2}\right\}p(t)\right)\right\}\\ \varepsilon_3 =& \left(\frac{R_i^2}{R_o^2-R_i^2}\right)\left\{\frac{\nu}{10E}-\frac{\nu}{E}\left(1+\frac{R_o^2}{r^2}\right)\right.\\ &\left.-\frac{\nu}{E}\left(1-\frac{R_o^2}{r^2}\right)\right\}p(t)\\ \varepsilon_3 =& \left(\frac{R_i^2}{R_o^2-R_i^2}\right)\left\{\frac{1}{10}-1-\frac{R_o^2}{r^2}-1+\frac{R_o^2}{r^2}\right\}\frac{\nu}{E}p(t)\end{aligned}$$

$$\varepsilon_3=\varepsilon_z=\frac{19\nu}{10E}\left(\frac{R_i^2}{R_i^2-R_o^2}\right)p(t). \tag{4}$$

Static pressures applied to the vessel comprised of two parts: a pressure applied to the interior walls outwards representing MAP (Mean Arterial Pressure), along with a pressure applied to the closed end of the vessel. Values for these are analogous to those in prior works [50, 51, 65]. That is, the MAP ($\bar{p}$) of 13.3 kPa(100 mmHg) was applied as the background arterial pressure, with systolic (maximum) pressure of 16 kPa(12 mmHg).

2.2.2 Dynamic models

Two dynamic studies were performed, the first being a benchmark using an applied pressure consisting of a sine wave over two realistic physiological time-periods, thus:

$$p(t)=\bar{p}+(p_s-p_d)\sin\left(\frac{2\pi}{T}t\right), \tag{5}$$

where p_s and p_d are the aforementioned systolic and diastolic pressures set respectively to 16 kPa and 10.5 kPa. The second dynamic study utilized interpolated pressures derived from measured velocity data (**Fig. 1**), determined in earlier work [35].

In the case of the latter, empirical data were acquired through measurement of flow using Doppler ultrasonography, with 2642 velocity values over a period of 1.32 s being obtained [35]. Assuming the minimum velocity value resulted from the diastolic pressure and the maximum velocity corresponded to the systolic pressure, a pressure profile acting on the interior walls was assumed (**Fig. 1**). Analytic values for this waveform were obtained via Fourier synthesis:

$$\begin{aligned}p(t)=&\frac{1}{2}a_o+\sum_{n=1}^{N}a_n\cos\left(\frac{2\pi}{T}t\right)\\ &+\sum_{k=1}^{N}b_n\cos\left(\frac{2\pi}{T}t\right),\end{aligned} \tag{6}$$

where T(= 0.66 s) was a physiologically realistic time period and $N > 64$ is the number of terms. The Fourier

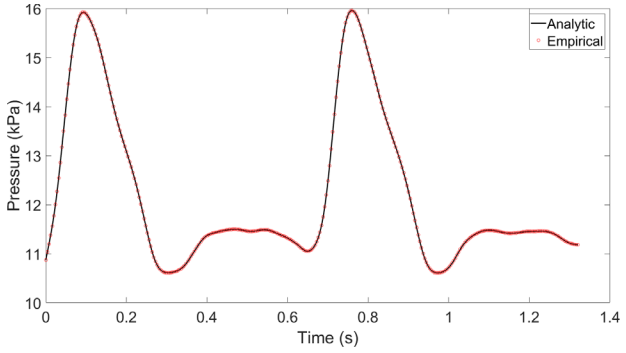

Fig. 1 Analytic and empirical pressure values interpolated from Wain *et al.* [35].

coefficients (a_n and b_n) were obtained from the Discrete Fourier Transform (DFT) of empirical data using the Fast Fourier Transform (FFT) algorithm resident in SciLab open-source data driven modelling software. The empirical data contained 2642 values thereby obtaining 1322 Fourier coefficients. **Figure 1** shows equation (6) is in excellent agreement with the empirical data.

2.2.3 Shear strain rate approximations

Whilst it is recognized that both the mechanical and fluid properties of these simulations are separate entities, and to model precise phenomena at the vessel walls would require a Fluid-Structural Interaction (FSI) analysis, we have calculated approximations of wall SSRs to provide an indication of the influence of compliance on this parameter. Here, for the pristine and coupled simulations, it was assumed that flow adhered to the Hagen-Poiseuille equation, was laminar and Newtonian, in keeping with existing studies [32, 33, 35].

Given these assumptions, differentiation of the Hagen-Poiseuille equation with respect to the spatial variable (r) renders:

$$\frac{\partial \mathrm{v}}{\partial \mathrm{r}}(r = R) = \dot{\gamma}(R) = \frac{-2\mathrm{v}_{\max}}{R},$$

where $\dot{\gamma}(R)$ is the SSR at the wall and $\mathrm{v}_{\max}$ is the maximum velocity of the blood. Since the inside radius of the vessel varies as a result of wall compliance and the applied pressure, application of this expression gives:

$$\dot{\gamma}(R) = \frac{-2\mathrm{v}_{\max}}{R_i(1 + \varepsilon_\theta)}. \tag{7}$$

Values of ε were found at systolic and diastolic pressures, when radial displacements were respectively maximal and minimal. Application of equation (7) therefore provides an approximation of SSR at the vessel wall for the pristine and coupled cases. Since the flow (and hence the SSR) is a localized effect at the sutures, estimations were made by application of a factor of 2.3 to the pristine case [35] for comparative purposes (**Table 3**).

2.3 Finite Element Analysis

In this work an assemblage of three-dimensional *ANSYS-SHELL181* elements [69] were employed for all models. These being iso-parametric elastic shell elements with six degrees of freedom (DoF), three displacements and three rotations, at each of the four nodes. The particular DoF between the nodes of each of the elements being interpolated from:

$$\varphi(x, y) = \sum_{i=1}^{4} N_i(\xi, \eta)\varphi_i, \tag{8}$$

where i is the local element number, φ_i is the value of the DoF at the ith node and $N_i(\xi, \eta)$ is the ith component of the bilinear quadrilateral vector, defined as:

$$\vec{N} = \frac{1}{4}[(1-\xi)(1-\eta), (1+\xi)(1-\eta), (1+\xi)(1+\eta), (1-\xi)(1+\eta)], \tag{9}$$

where ξ and η are local abscissa and ordinate coordinates originating at the element centroid.

The ANSYS software therefore constructs a structural stiffness matrix [***K***] via application of:

$$[K] = \sum_{i=1}^{n} [A]^T k_i [A], \tag{10}$$

where $[A]$ is the so-called assembly matrix[2]. This being representative of the elastic response of the structure given applied loads and Robin boundary conditions [72–74] which are applied to appropriate nodes. Thereby in adherence to generalized Hooke's Law [75]:

$$\{F\} = [K]\{u\}, \tag{11}$$

where $\{F\}$ is a vector of applied forces at the nodes and $\{u\}$ is the displacement vector. Herein a displacement based method is employed, whence $\{u\}$ is determined from either direct (*Frontal*) or partial (*Sparse direct*) inversion of equation (10).

For time-varying (dynamic) loading, Newton's second law of motion was applied:

$$\{F\} = [K]\{u\} + [M]\{\ddot{u}\}, \tag{12}$$

where vectors $\{u\}, \{\ddot{u}\}$ and $\{F\}$ are time-dependent displacement, acceleration and force respectively and $[M]$ is the mass matrix for the body.

Equation (12) was solved using the Newmark-β method [76], this being a weighted implicit finite difference scheme:

$$\{\dot{u}_{n+1}\} = \{\dot{u}_n\} + \{(1-\gamma)\{\ddot{u}_n\} + \gamma\{\ddot{u}_{n+1}\}\}\Delta t$$

$$\{u_{n+1}\} = \{u_n\} + \{\dot{u}_n\}\Delta t + \left\{\left(\frac{1}{2} - \beta\right)\{\ddot{u}_n\} + \beta\{\ddot{u}_{n+1}\}\right\}\Delta t^2,$$

in order to approximate the displacement at each of the nodes in the mesh. Here β and γ are weighting coefficients, ensuring convergence of the numerical scheme, termed the Newmark integration parameters. In the work that follows, β and γ were set by the ANSYS software to 0.25 and 0.5 respectively, thereby ensuring unconditional stability [69].

2.3.1 Pristine vessel models

These surface models were produced in the DesignModeler of ANSYS-Workbench simulation suite. Here, two lines were initially constructed. The first being 1.25 mm, and second 15 mm, located at the end point of the first, and perpendicular to it. The former length corresponding to the characteristic radius of the vessel, with the latter

[2] The ANSYS software makes use of sophisticated element assembly routines [54] meaning this is not evaluated explicitly.

being the effective length of the vessel. The *revolve* command was employed, together with a suitable principal axis, to produce the required surface with a thickness of 0.25 mm applied to complete the model (**Fig. 2**).

In this case, a mapped mesh is more appropriate as the mesh can be controlled and refined manually. Here, the structured mapped mesh consisted of 100 divisions along the vessel length and 40 divisions around its circumference (**Fig. 3**). The mesh comprised 6278 nodes, with 6104 elements, corresponding to 36500 DoF.

A zero rotation condition was placed upon the two lengths, along with a restricted displacement in the longitudinal and radial directions; allowing for movement in the circumferential direction. Upon the open end of the vessel, a fixed support was added in order to analyze movement of the main body alone.

For the static structural models described, the *Frontal Solver* was employed, and for transient problems, the *Sparse Direct Solver* was used as per the ANSYS default settings. Evaluation of inertial effects were anticipated in the dynamic study with a higher likelihood of non-linear solutions compared to the static structural models. Alongside these, so-called *weak springs* were activated. The addition of these helped prevent numerical instabilities, although had no effect on the reaction forces. Additionally, the *large deflection* control setting was applied, as preliminary static analysis showed global strain calculations exceeded 10%, implying large geometric changes.

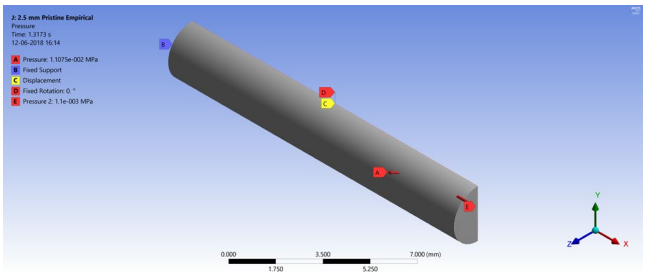

Fig. 2 Pristine vessel geometry detailing boundary conditions.

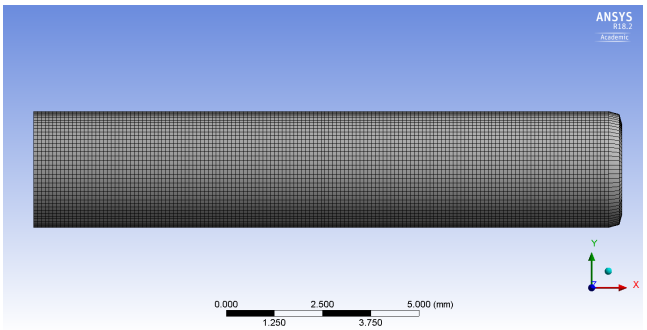

Fig. 3 Pristine vessel mesh.

2.3.2 Sutured anastomosis models

For an artery of 2.5 mm diameter, approximately eight sutures are required to perform a well-sealed microanastomoses [6, 33]. As such, eight evenly spaced suture sites were placed around the circumference of the vessel geometry, each measuring ~0.04 mm, in-keeping with the values described in Section 1. The geometry thus created can be seen in **Figs. 4a and 4b**.

Sutured geometries consisted of two cylinders of identical principal dimensions, as described in the previous section, connected end-to-end via the *spot-weld* tool within ANSYS DesignModeler. The spot-weld feature adjoins two bodies via dictated vertices and nodes (**Fig. 5**). This technique is similar to that used by Ballyk *et al*. [40] and Perktold *et al*. [48] in their FEA studies.

A similar meshing stratagem to that of the pristine vessel was used, although 50 elements were placed around the circumferential edge of the vessel to compensate for lack of mesh uniformity due to the spot-welds (**Fig. 5**). Whilst the majority of the model is comprised of relatively large elements (≃0.6) mm, a high density mesh is concentrated around suture sites. This was achieved using a *sphere of influence* to ensure a locally converged solution (seen in more detail in **Fig. 9a**). The mesh applied consisted of 8370 elements with 8725 nodes, corresponding to approximately 50000 DoF.

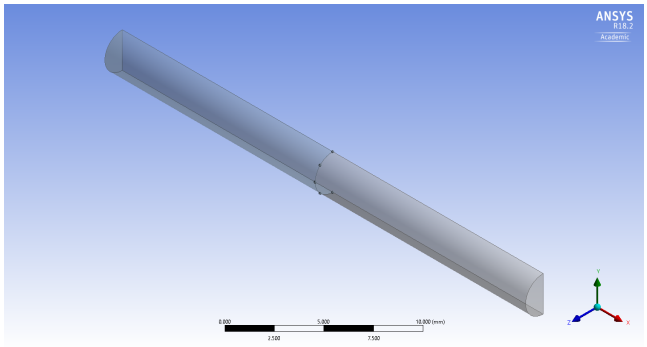

(a) Sutured anastomosis geometry isometric view

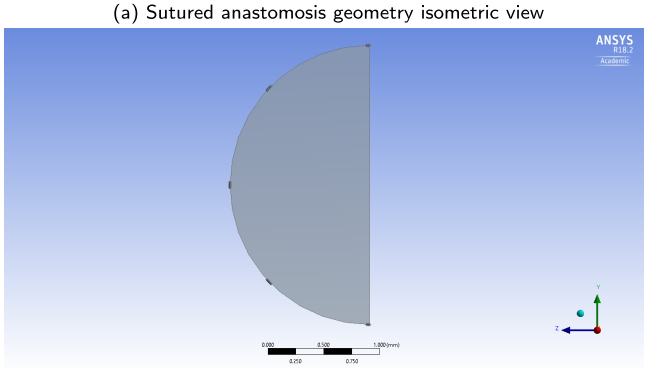

(b) Sutured anastomosis geometry planar view

Fig. 4 Sutured microanastomosis geometry demonstrating even distribution of sutures in both (a) isometric and (b) planar views.

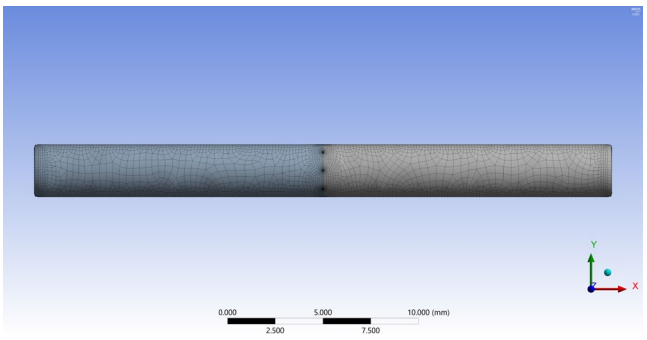

Fig. 5 Sutured anastomosis mesh of the whole geometry demonstrating higher mesh density at suture sites created using the spot weld function.

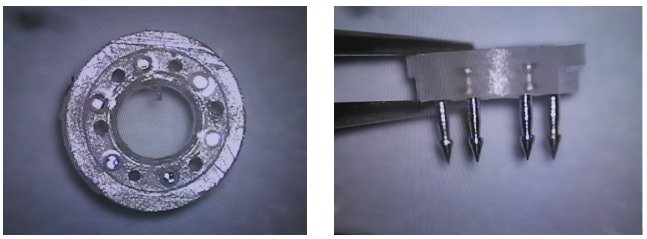

(a) Front coupler view (b) Side coupler view

Fig. 6 Micrographs demonstrating the GEM Microanastomotic Coupling (MAC) device from both (a) front and (b) side views (sourced from [32]).

Boundary conditions applied were identical to those of the pristine vessel.

2.3.3 Coupled anastomosis models

The surface model was composed using many of the same principles as the pristine geometry. However, at the anastomotic site, a rendered stretched arterial wall (fillet radius of 0.25 mm and length 3 mm) was added to represent vessel wall eversion with the coupling device *in situ* (*i.e*. vessel walls reflected backwards and passed over the pins). **Figure 6** demonstrates micrographs of the coupling device through which vessel ends are passed. The full computational geometry used is shown in **Fig. 7**.

Meshing of the coupled model also utilized a mapped mesh, however the face mapped mesh was also applied at the coupling site (**Fig. 8**). Over the long edges of the vessel 100 divisions were used. In addition, 20 divisions were applied on the curved face of the model to increase mesh density in the area of interest. A single side of the anastomosis was simulated in the FEA models as the solution was expected to be symmetric. The mesh applied consisted of 3208 elements with 3362 nodes, corresponding to 18000 DoF.

Boundary conditions applied to the coupled anastomosis model were identical to those of the pristine vessel, however a *fixed support* was applied at the coupling site to simulate the device holding the arterial walls fixed in place, as would be the case *in vivo*.

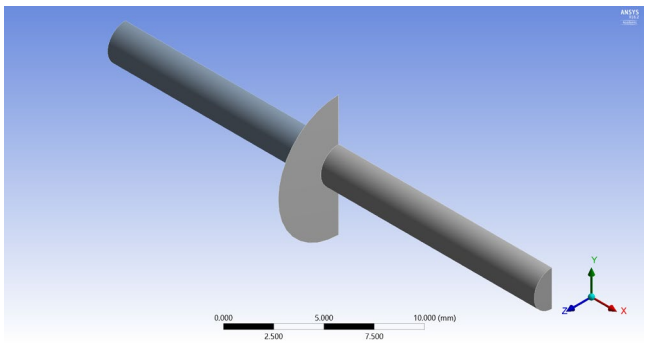

Fig. 7 Coupled anastomosis geometry isometric view.

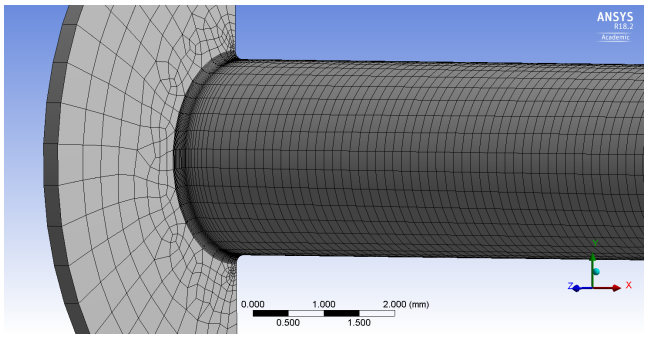

Fig. 8 Coupled anastomosis mesh demonstrating refinement at the anastomotic site.

3. Results and discussion

This section initially presents and discusses the results for all static analyses. Here, pristine simulations are demonstrated in the context of analytic solutions, before discussion focusses on the influence of sutured and coupled anastomotic techniques on the stress and strain distributions. Attention is then directed to transient solutions of identical models. Here, displacement plots are shown evaluating a sinusoidally varying pressure and, subsequently, a realistic empirical pulsatile waveform in pristine vessels. The pulsatile pressure profile is then applied to each of the anastomotic techniques, and respective stress, strain and failure criteria are discussed. Finally, comparisons are drawn between these FEA simulations and those of previously published CFD approximations.

3.1 Static analyses

This section describes results of the non time-dependent simulations for each geometrical model, and provides discussion of their accuracy and potential significance. Pristine simulations are addressed first, to provide a baseline of the natural state of the vessel, with both su-

tured and coupled models discussed subsequently.

3.1.1 Pristine vessel

Results for the pristine vessel's deformation, maximum principal strain, and maximum principal stress are shown in **Table 1**. The maximum principal stress is 79.8 kPa which is in agreement the aforementioned Lamé-Clapeyron cylinder theory. Using the applied static pressure of 16 kPa as the intra-arterial pressure, the expected analytic value calculates to 88.7 kPa. Further verification for the ANSYS Structural static results is seen in **Table 1**. Here, a value of ~17.2% is shown for the FEA value of ε_1, which is identical to the value of 17.2% obtained using equation (3). The radial displacement values will be further discussed in section (3.2.1), although these are also in good agreement.

3.1.2 Sutured anastomosis

The values of stress and strain directly at suture sites are zero, as expected through application of the spot-weld condition. Areas surrounding the suture, and therefore under its influence, reach values of ~31.7% maximum principal strain and 160 kPa maximum principal stress. *These values are almost double those of the pristine model*. **Figure 9** shows strain distributions at the anastomotic site. It can be seen here that maximum values are found immediately adjacent to suture sites along the circumference of the anastomosis, rather than at sutures themselves. This would be expected as greatest strains would be experienced next to a fixed support, in this case the spot-weld of the suture, thereby predicting failure at this point in the case of high displacement.

It is clear from **Fig. 9** that gaps are visible between suture sites when the intra-arterial pressure is at its maximal value. These gaps are small (~20 μm) and are less than the vessel wall thickness (250 μm) and as such blood is unlikely to leak from these apertures. Larger gaps with less, or poorly placed, sutures would however permit blood to escape.

It is important to consider that the simulations performed herein represent those of the surgical picture *immediately* after the anastomosis has been performed *i.e.* before any healing has occurred by the body's natural processes. As such, the gapping and resultant strain distributions seen in **Fig. 9** are as expected with radial displacement. However, these differ markedly from those found by Ballyk *et al.* [40] and Perktold *et al.* [48]. In particular, no gapping was seen, and maximum strain distributions were found to be along the longitudinal axis of the vessel rather than along the circumference of the anastomosis itself. We therefore postulate that the afore-

Table 1 Analytic and ANSYS Static FEA absolute value comparisons for a pristine vessel model.

Variable (maximum)	Analytic	ANSYS Static FE
Total deformation [μm]	680	641
Radial deformation [μm]	238	220
Longitudinal deformation [μm]	637	588
First principal strain [%]	17.2	17.2
Second principal strain [%]	4.67	4.10
First principal stress [kPa]	88.7	79.8
Second principal stress [kPa]	3.6	3.7

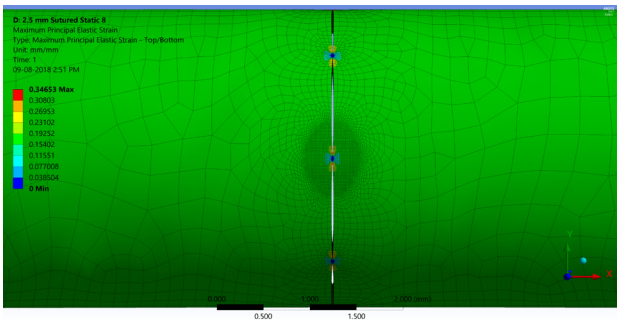

(a) Sutured anastomosis model maximum principal strain distribution showing three suture sites with the central suture demonstrating a *sphere of influence* mesh refinement

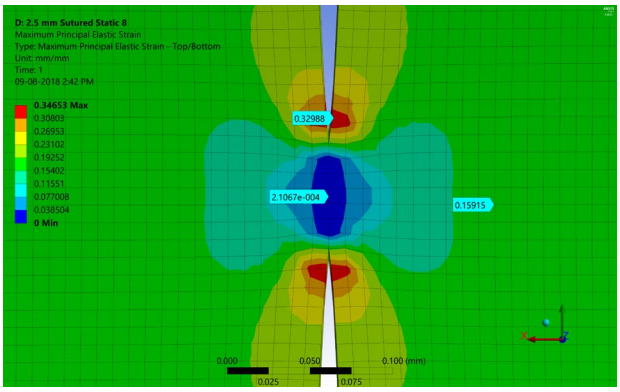

(b) Sutured anastomosis model maximum principal strain around central suture site

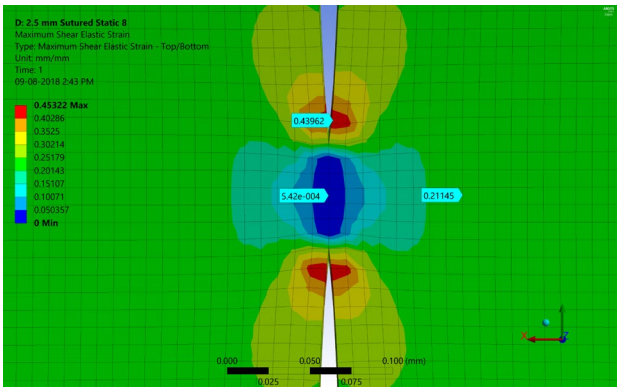

(c) Sutured anastomosis model maximum shear strain around central suture site

Fig. 9 Sutured anastomosis model static strains (ε).

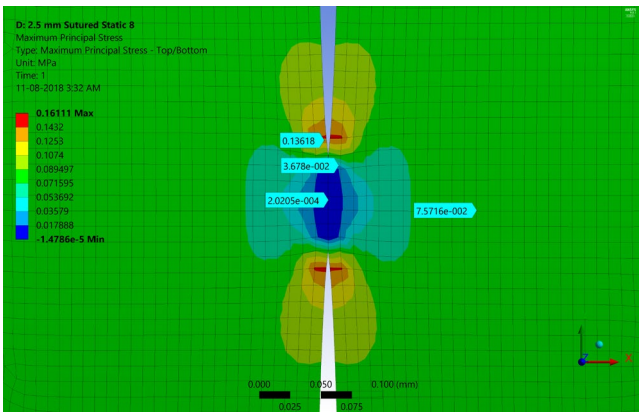

(a) Maximum principal stress distribution of an *unhealed* suture site (σ_1)

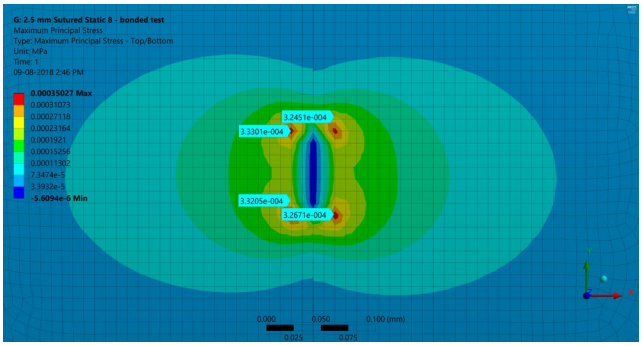

(b) Maximum principal stress distribution of a *healed* suture site (σ_1)

Fig. 10 Comparison of stress distributions in end-to-end sutured anastomoses for both (a) *unhealed* and (b) *healed* vessels showing the influence of a bonded connection.

mentioned studies applied a *bonded connection* to each end of the vessel and *then* applied spot-welds, thereby representing a *healed* anastomosis and altering the resultant strain distributions.

We performed comparative simulations of stress in both *unhealed* and *healed* anastomoses to test this assumption. As would be expected, the strain field presented in **Fig. 9** is strongly analogous to the stress field in the *unhealed* sutured anastomosis model (**Fig. 10a**), demonstrating the same degree of gapping. Again, the maximum strain occurs not at suture points themselves, but either side of the point of coalescence. Upon application of a *bonded connection* to the anastomotic site of an otherwise identical simulation, thereby representing a *healed* anastomosis, a significantly different stress distribution is seen (**Fig. 10b**). Here, maximum values are found in closer proximity to suture sites with the remaining higher stresses experienced in the longitudinal axis, more akin to that found by Ballyk *et al.*[3] [40]. It therefore being demonstrated that application of a *bonded connection* is likely in the works of Ballyk *et al.* [40] and Perktold *et al.* [48].

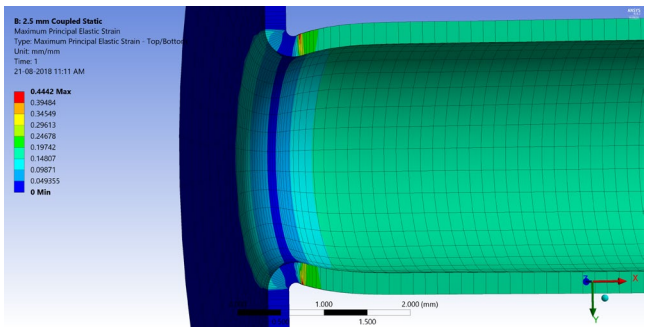

(a) Coupled anastomosis model maximum principal strain

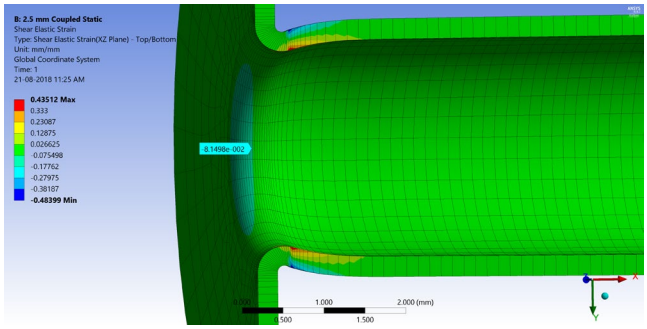

(b) Coupled anastomosis model maximum shear strain

Fig. 11 Coupled anastomosis model static maximum strains (ε).

3.1.3 Coupled anastomosis

Around the radius of the coupled section, stresses and strains tend to be lower, as can be seen in **Fig. 11**, whilst the main body of the arterial wall demonstrates values close to those for the pristine artery (**Table 1**). Maximum principal and maximum shear strains are depicted in **Figs. 11a and 11b** respectively. The lowest values can be seen around the interior curvature of the wall, with maximum principal strain values of ~7.7% and maximum shear strain values of ~8.1%. *These represent strain values approximately half that seen in pristine vessels, and less than one third of those found in the sutured anastomosis.*

For the radius caused by bending the vessel around the coupling device, maximum stress and strain values are seen at the boundary of the radius. This is a result of the boundary conditions applied. Specifically, fixing the everted vessel at the coupling site permits high strain concentrations adjacent to this point due to the internal pressure exerted on the interior radius. This would not be the case in clinical practice however, as the vessel is fixed by pins between polyethylene rings and as such the point at which the vessel exits the ring is mobile.

It is clear from comparing the strain values seen in coupled anastomoses (**Fig. 11**) with those of sutured

[3] Figures for comparison can be found at: https://www.sciencedirect.com/science/article/pii/S0197397597001115

anastomoses (**Fig. 9**) that values are notably higher in the sutured vessels. Should anastomoses fail by these mechanisms, it could be inferred that the sutured anastomosis would be more likely to fail than a coupled one. This is in-keeping with clinical findings of lower failure rates in venous coupled anastomoses compared to sutured [3, 77], although the principal mechanism underlying failure, and whether the same would be true for arteries, is less clear. These findings may have implications for novel device design.

3.2 Transient analyses

In this section we discuss the results obtained when time-dependent pressure profiles were applied to identical geometries. For verification purposes a sinusoidal waveform was employed in the first instance, with a physiologically realistic arterial pulse applied thereafter.

3.2.1 Sinusoidal waveform

Figure 12a shows displacement of the pristine arterial model when a sinusoidal pressure profile is applied. This sine wave varies between the expected systolic and diastolic pressures *in vivo* over a period of 1.4 s Here, very good agreement is demonstrated between the analytic and mean FE model predictions. This mean being calculated from measurements of ten evenly-spaced points around the circumference of each model. The analytic curve falls within the error bars, calculated at the 95% confidence level [78], with respect to the mean FE values. The maximum value from the ANSYS FEA being ~225 μm, whilst the maximum analytic result is 220 μm, again demonstrating good agreement. These results permit application of this technique to a realistic waveform [35] (**Fig. 12b**).

3.2.2 Physiological waveform

Maximum principal strain values are shown in **Fig. 13**. Here these data are compared with analytic model ana-

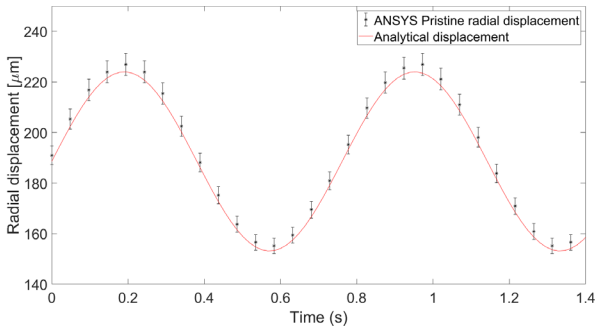

(a) Pristine artery model, displacement due to sinusoidal pressure profile. Error bars represent the 95 % confidence interval

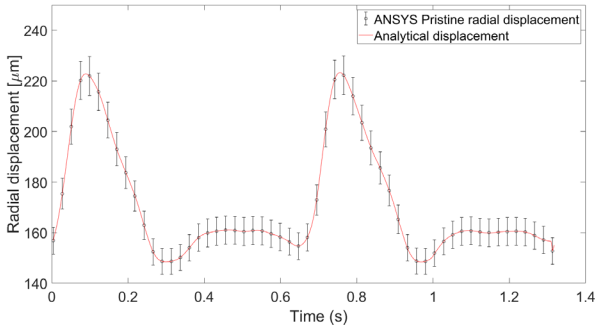

(b) Pristine artery model, displacement due to empirical pressure profile. Error bars represent the 95 % confidence interval

Fig. 12 Pristine artery model radial displacement with both (a) sinusoidal and (b) empirical realistic pulsatile pressure profiles.

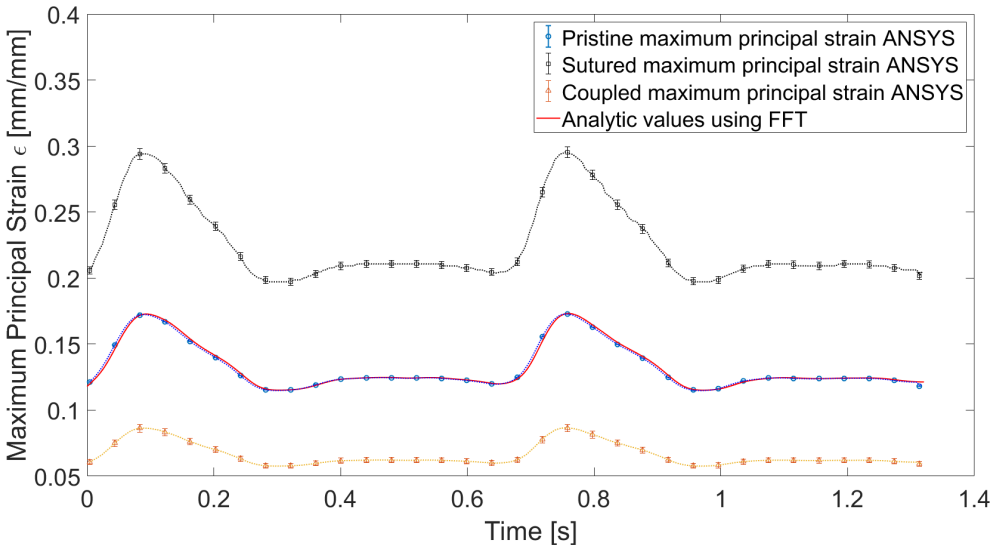

Fig. 13 Comparative plot showing maximum principal strain FEA predictions in pristine vessels and microanastomoses with application of a time-dependent physiological pressure profile. Analytic results are also shown.

logues over identical time periods. For the sutured anastomosis, elements were taken at the high stress areas around the suture sites. For the coupled model, the area of interest was the arterial wall at the coupling device, where eversion and coaptation occurs. As with the sinusoidal waveform, a sample of ten evenly-spaced point values were taken around the inside radius (**Fig. 11**), and the mean calculated at the 95% confidence level. In each of these cases the analytic solution is in good agreement with the FEA approximations. It can be seen in **Fig. 13** that the coupling device demonstrates much lower principal strains than the sutured model, and even the pristine vessel, with identical loading pressures. When the sutured model is compared directly to that of the pristine vessel, consistently higher values for maximum principal strain are predicted. Due to the arterial walls approximating to a laminate composite material physiologically, and there being no distinct stress-strain response available, the maximum strain failure criterion is deemed the most appropriate.

These results show that the coupling device outperforms conventional sutures in arteries of 2.5 mm. Should failure occur due to principal strains, it would be at, or more likely above, the maximum value achieved here. At systolic pressure the average maximum principal strain of the sutured model is around 32% representing an increase from 17.2% in the pristine case. Failure at this pressure is unlikely as these are the pressures seen physiologically in normal vessels of this nature. In line with salient engineering pressure vessel codes [79], so-called plastic collapse of the anastomotic vessel is predicted at strains ~40%, corresponding to $2t/\bar{R}$.

At strains of this magnitude the assumptions of linear elasticity (as simulated here) tend to be inappropriate. However, **Fig. 14** shows that both the Neo-Hookean and Mooney-Rivlin hyperelastic models predict very similar failure strains; thereby verifying our use of the Maximum Failure Strain criterion. Here the Neo-Hookean shear modulus and incompressibility factor were evaluated from the isotropic relations, namely:

$$\frac{2}{K} = \frac{6(1-2\nu)}{E}$$

and

$$G = \frac{E}{2(1+\nu)}.$$

On the other hand, for the Mooney-Rivlin model, this was calculated from:

$$G = 2(E_{01} + E_{10})$$

with the elastic constants E_{01} and E_{10} being determined from least-squares estimates of an initially imposed linear elastic response up to 1% strain; with the L1-norm limited to 0.05 with respect to the Hookean model. These results show that the failure strain prediction of the two hyperelastic models is between ~38% and ~43% respectively. However, it should also be pointed out that over these particular strains, the resulting difference in stress values are ~17% and ~43% respectively. It becomes obvious that further work in this area is required.

Given these quite specific failure conditions, our results show that the sutured model will likely cause an increase in gap size at the anastomotic site, and hence leakage. Experimental studies confirm that leakage would be the first sign of failure [80]. Furthermore, in pathological conditions, there is also the distinct possibility of vessel wall tearing, particularly in friable vessels of post-radiotherapy patients or in traumatic injuries, at strains of this magnitude. This has significant implications in potential for vessel failure and may favour a coupling device based on the data seen herein.

Comparisons of the transient models with their static analogues (**Table 2**) reveals very similar extrema values for each of the salient calculations. Here, good agreement is demonstrated between the two approaches. The correlations observed provide clear evidence that for the vessels simulated here, the so-called inertial effects are minimal, particularly in the case of the pristine arterial model.

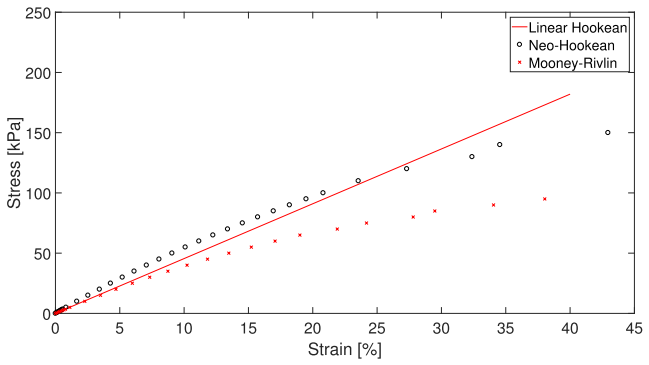

Fig. 14 Comparison of linear elastic and hyperelastic material responses.

3.3 SSR comparisons with CFD

Table 3 shows values obtained for SSR using the method described in section (2.2.3) for each of the anastomotic

Table 2 Comparison of static and transient strain predictions for each vessel model.

Model	Static strain (%)	Transient strain (%)	Difference (%)
Pristine	17.2	17.3	0.58
Sutured	31.7	29.6	7.09
Coupled	7.7	8.1	4.93

Table 3 Calculated SSR approximations (s^{-1}) in compliant vessels. Comparison of pristine artery, sutured and coupled microarterial anastomoses for minimum, maximum and average values of strain in transient simulations.

SSR	Pristine vessel	Coupled anastomosis	Sutured anastomosis
SSR (diastolic)	1192	1053	2742
SSR (MAP)	992	972	2282
SSR (systolic)	845	912	1944

techniques. As would be expected, the pristine vessel SSR approximates to the value obtained in Hagen-Poiseuille flow (992 s^{-1}) in each case, with variation corresponding to changes in strain at the extremes of intra-arterial pressure. In the case of the coupled vessel, it should be noted that the coupler is rigid, and as such would reduce vessel expansion and contraction at the anastomotic site. Therefore, variation seen in SSRs throughout the cardiac cycle is *less* compared to the pristine case, with overall SSR profiles being of similar magnitude. This is in keeping with an earlier study using CFD [32]. Sutured vessels however, demonstrate much higher SSR values throughout. The relationship between these SSR values is consistent with those found in the rigid-walled CFD models [32, 33, 35], and as such it could be hypothesized that compliance does not significantly affect predictions of SSR in these vessels.

It is important to highlight, however, that SSR variations here are taken in isolation, and that changing pressure gradients are likely to produce much greater variation in vessel wall strain values than the influence of fluid flow alone. Hence, a formal fluid-structure interaction (FSI) study would be necessary to ascertain the true relationship.

4. Conclusions

Although idealized in many respects, this study represents the first FE predictions comparing stress and strain distributions in sutured and coupled microarterial anastomoses. Analytic and FE models have been produced to predict the elastic response of microvessels in pristine and repaired forms. In particular, unlike other studies, these models have specifically evaluated mechanical failure properties at the anastomotic site immediately after surgery (*i.e.* in the *unhealed* anastomosis) so as to best represent the physiological and surgical picture. The salient technical and clinical conclusions being as follows.

- Thick-wall cylinder theory is a suitable and appropriate strategy for representing models of pristine microarteries analytically.
- The *spot weld* function available in ANSYS DesignModeler can be employed to simulate joining vessels with surgical suture material, at least in idealized simulations, as the number of nodes can be approximated to the diameter of the suture material itself. Further work could be carried out here to incorporate material properties of nylon or polypropylene, in addition to a full FSI model.
- A Fourier series representation of measured human arterial pulse waves can be reliably created using the FFT algorithm within SciLab software. This can subsequently be employed as a time-dependent pressure-driven boundary condition for these compliant vessel models.
- Excellent agreement has been demonstrated for the displacement fields, and hence derived quantities such as stress and strain, between the FE and analytic pristine vessel models.
- The maximum principal strain in a sutured anastomosis is approximately 84% greater than in a pristine vessel, and around 3-fold that of a coupled anastomosis. As this has been assumed the most likely failure criterion, these findings provide evidence that a sutured anastomosis is more likely to fail than a coupled one, which is in keeping with findings seen clinically and in similar research.
- Simulating the sutured anastomosis in the way described herein is more representative of the clinical picture *immediately* following surgery (*i.e.* permits a degree of anastomotic separation due to radial displacement). This is in contrast to that performed by other groups [40, 48], where conditions more closely represent that of a *healed* anastomosis and as such the strain distributions are quite different.
- The inertial effects due to the motion of the vessel during pulsatile flow are minimal, since the differences between the transient and static strain calculations range from around 0.6–7% dependent on the geometry. That is, for the waveform investigated here, the dynamic response is completely characterized by the static elastic response of the vessel walls. This implies that static structural analyses are sufficient to predict anastomotic failure, and as such to optimize future device design.
- Both FE and analytic models predict natural background strain levels of 17.2%. Given strain values calculated in the sutured models (~30%), we suggest that average maximum principal strains significantly greater than this (~40%), would be required to represent anastomotic failure.
- An approximation of the SSR has been calculated at anastomotic sites in an attempt to compare findings of

these compliant simulations with values obtained in rigid-walled CFD simulations of analogous vessels. Whilst SSR variation is seen during the cardiac cycle, it appears the relationship between each type of anastomosis, and the overall magnitude of the SSRs is largely unaffected by application of the compliant wall condition.

Acknowledgements

The authors wish to express their thanks to the Vascular Studies Unit at the University Hospital of South Manchester NHS Foundation Trust, for providing anonymised vascular data for creation of inlet profiles and geometries. The authors also wish to express their thanks to the members of the Multi-scale Biology Study Group, University of Birmingham (December 2017) for their valuable discussions regarding this subject.

Conflict of interest

The authors declare they have no conflicts of interest.

Funding

The authors declare no specific funding for this manuscript. The Multi-scale Biology Study Group, University of Birmingham (December 2017) was jointly funded by POEMS (Predictive modelling for healthcare technology through maths - EP/L001101/1) and MSB-Net (UK Multi-Scale Biology Network - BB/M025888/1).

Contribution

All authors contributed to the design of the research, analysis of the data, and writing of this manuscript. NG & RW constructed the geometries, performed the simulations, and analysed the data. NG, RW & JW compiled the manuscript. JW, AF & JF provided technical assistance, mathematical support and overall supervision of the project.

References

1. Wain RAJ, Hammond D, McPhillips M, Whitty JPM, Ahmed W, Microvascular Anastomoses: Suture and Non-suture Methods, in: Ahmed W, Jackson MJ (Eds.), Surgical Tools and Medical Devices, Springer International Publishing, 2016, pp. 545–562.
2. Yap LH, Constantinides J, Butler CE, Venous thrombosis in coupled versus sutured microvascular anastomoses. Ann Plastic Surg. **57** (6), pp. 666–669, 2006.
3. Jandali S, Wu LC, Vega SJ, Kovach SJ, Serletti JM, 1000 consecutive venous anastomoses using the microvascular anastomotic coupler in breast reconstruction, Plastic Reconstructive Surg. **125** (3), pp. 792–798, 2010.
4. Ardehali B, Morritt AN, Jain A, Systematic review: anastomotic microvascular device, J Plastic, Reconstructive Aesthetic Surg. **67** (6), pp. 752–755, 2014.
5. Wain RAJ, Whitty JPM, Ahmed W, Microvascular coaptation methods: device manufacture and computational simulation, in: Jackson MJ, Ahmed W (Eds.), Micro and Nanomanufacturing, Vol. 2, Springer, 2018, pp. 545–559.
6. Alghoul MS, Gordon CR, Yetman R, Buncke GM, Siemionow M, Afifi AM, Moon WK, From simple interrupted to complex spiral: a systematic review of various suture techniques for microvascular anastomoses. Microsurgery. **31** (1), pp. 72–80, 2011.
7. Payr E, Beitrage zur Technik der blutgefass- und Nervennaht nebst Mittheilungen uber die Verwendung eines resorbirbaren Metalles in der Chirurgie. Arch Klin Chir. **62**, p. 67, 1900.
8. Nakayama K, Tamiya T, Yamamoto K, Akimoto S: A simple new apparatus for small vessel anastomosis (free autograft of the sigmoid included). Surgery. **52** (6), pp. 918–931, 1962.
9. Ostrup LT: Anastomosis of small veins with suture or Nakayama's apparatus. A comparative study. Scandinavian J Plastic Reconstructive Surg. **10** (1), pp. 9–17, 1976.
10. Ostrup LT, Berggren A: The UNILINK instrument system for fast and safe microvascular anastomosis. Ann Plastic Surg. **17** (6), pp. 521–525, 1986.
11. Rozen WM, Whitaker IS, Acosta R: Venous Coupler for Free-Flap Anastomosis: Outcomes of 1,000 Cases. Anticancer Res. **30** (4), pp. 1293–1294, 2010.
12. Ross DA, Chow JY, Shin J, Restifo R, Joe JK, Sasaki CT, Ariyan S: Arterial coupling for microvascular free tissue transfer in head and neck reconstruction. Arch Otolaryngology-Head Neck Surg. **131** (10), pp. 891–895, 2005.
13. Chernichenko N, Ross DA, Shin J, Chow JY, Sasaki CT, Ariyan S: Arterial coupling for microvascular free tissue transfer. Otolaryngol Head Neck Surg. **138** (5), pp. 614–618, 2008.
14. Spector JA, Draper LB, Levine JP, Ahn CY: Routine use of microvascular coupling device for arterial anastomosis in breast reconstruction. Ann Plastic Surg. **56** (4), pp 365–368, 2006.
15. Uenal N, Klein U, Höpken M, Maune S: P26 The utility of coupler devices for arterial anastomosis in free tissue transfer. Oral Oncol. **51** (5), pp. e50, 2015.
16. Kroll SS, Schusterman MA, Reece GP, Miller MJ, Evans GR, Robb GL, Baldwin BJ: Choice of flap and incidence of free flap success. Plastic Reconstructive Surg. **98** (3), pp. 459–463, 1996.
17. Khouri RK, Cooley BC, Kunselman AR, Landis JR, Yeramian P, Ingram D, Natarajan N, Benes CO, Wallemark C: A prospective study of microvascular free-flap surgery and outcome. Plastic Reconstructive Surg. **102** (3), pp. 711–721, 1998.
18. Bellidenty L, Chastel R, Pluvy I, Pauchot J, Tropet Y: Emergency free flap in reconstruction of the lower limb. thirty-five years of experience. Ann De Chirurgie Plastique Et Esthetique. **59** (1), pp. 35–41, 2014.
19. Beugels J, Hoekstra LT, Tuinder SMH, Heuts EM, van der Hulst RRWJ, Piatkowski AA: Complications in unilateral versus bilateral deep inferior epigastric artery perforator flap breast reconstructions: A multicentre study. J Plastic, Reconstructive Aesthetic Surg. **69** (9), pp. 1291–1298, 2016.
20. Bendon CL, Giele HP: Success of free flap anastomoses performed within the zone of trauma in acute lower limb reconstruction. J Plastic, Reconstructive Aesthetic Surg. **69** (7), pp. 888–893, 2016.
21. Mustard JF, Murphy EA, Rowsell HC, Downie HG: Factors influencing thrombus formation in vivo. Am J Med. **33** (5), pp. 621–647, 1962.

22. Lowe GDO: Virchow's triad revisited: abnormal flow. Pathophysiol Haemostasis Thrombosis. **33** (5–6), pp. 455–457, 2003.
23. Roth GJ: Developing relationships: arterial platelet adhesion, glycoprotein Ib, and leucine-rich glycoproteins. Blood. **77** (1), pp. 5–19, 1991.
24. Kroll MH, Hellums JD, McIntire LV, Schafer AI, Moake JL: Platelets and shear stress. Blood. **88** (5), pp. 1525–1541, 1996.
25. Hathcock JJ: Flow effects on coagulation and thrombosis. Arteriosclerosis, Thrombosis, and Vascular Biology. **26** (8), pp. 1729–1737, 2006.
26. Shen F, Kastrup CJ, Liu Y, Ismagilov RF: Threshold response of initiation of blood coagulation by tissue factor in patterned microfluidic capillaries is controlled by shear rate. Arteriosclerosis, Thrombosis, and Vascular Biology. **28** (11), pp. 2035–2041, 2008.
27. Sakariassen KS, Nievelstein PF, Coller BS, Sixma JJ: The role of platelet membrane glycoproteins Ib and IIb-IIIa in platelet adherence to human artery subendothelium. Br J Haematol. **63** (4), pp. 681–691, 1986.
28. Grabowski EF: Platelet aggregation in flowing blood at a site of injury to an endothelial cell monolayer: quantitation and real-time imaging with the TAB monoclonal antibody. Blood. **75** (2), pp. 390–398, 1990.
29. Bark DL Jr, Para AN, Ku DN: Correlation of thrombosis growth rate to pathological wall shear rate during platelet accumulation. Biotechnol Bioeng. **109** (10), pp. 2642–2650, 2012.
30. Steinman DA: Assumptions in modelling of large artery hemodynamics, in: Ambrosi D, Quarteroni A, Rozza G (Eds.), Modeling of Physiological Flows, Springer Milan, 2012, pp. 1–18.
31. Wain RAJ: Computational modelling of blood flow through sutured and coupled microvascular anastomoses, Master of Science, by Research, University of Central Lancashire (Apr. 2013).
32. Wain RAJ, Whitty JPM, Dalal MD, Holmes MC, Ahmed W: Blood flow through sutured and coupled microvascular anastomoses: a comparative computational study. J Plastic, Reconstructive Aesthetic Surg. **67** (7), pp. 951–959, 2014.
33. Wain RAJ, Hammond D, McPhillips M, Whitty JPM, Ahmed W: Microarterial anastomoses: A parameterised computational study examining the effect of suture position on intravascular blood flow. Microvasc Res. **105**, pp. 141–148, 2016.
34. Whitty JPM, Wain RAJ, Fsadni A, Francis J: Computational Non-Newtonian Hemodynamics of Small Vessels. J Bioinf Comput Syst Biol. **1** (1), p. 103, 2016.
35. Wain RAJ, Smith DJ, Hammond D, Whitty JPM: Influence of microvascular sutures on shear strain rate in realistic pulsatile flow. Microvasc Res. **118**, pp. 69–81, 2018.
36. Migliavacca F, Dubini G: Computational modeling of vascular anastomoses. Biomech Modeling Mechanobiol. **3** (4), pp. 235–250, 2005.
37. Steinman DA, Taylor CA: Flow imaging and computing: large artery hemodynamics. Ann Biomed Eng. **33** (12), pp. 1704–1709, 2005.
38. Trubel W, Moritz A, Schima H, Raderer F, Scherer R, Ullrich R, Losert U, Polterauer P: Compliance and formation of distal anastomotic intimal hyperplasia in Dacron mesh tube constricted veins used as arterial bypass grafts. Am Soc Artificial Int Organs J. **40** (3), pp. 273–278, 1994.
39. Hofer M, Rappitsch G, Perktold K, Trubel W, Schima H: Numerical study of wall mechanics and fluid dynamics in end-to-side anastomoses and correlation to intimal hyperplasia. J Biomech. **29** (10), pp. 1297–1308, 1996.
40. Ballyk PD, Walsh C, Butany J, Ojha M: Compliance mismatch may promote graft-artery intimal hyperplasia by altering suture-line stresses. J Biomech. **31** (3), pp. 229–237, 1997.
41. Abbott WM, Megerman J, Hasson JE, L'Italien G, Warnock DF: Effect of compliance mismatch on vascular graft patency. J Vasc Surg. **5** (2), pp. 376–382, 1987.
42. Samaha FJ, Oliva A, Buncke GM, Buncke HJ, Siko PP: A clinical study of end-to-end versus end-toside techniques for microvascular anastomosis: Plastic Reconstructive Surg. **99** (4), pp. 1109–1111, 1997.
43. Head C, Sercarz JA, Abemayor E, Calcaterra TC, Rawnsley JD, Blackwell KE: Microvascular reconstruction after previous neck dissection. Archives of Otolaryngology-Head & Neck Surgery. **128** (3), pp. 328–331, 2002.
44. Nahabedian MY, Singh N, Deune EG, Silverman R, Tufaro AP: Recipient vessel analysis for microvascular reconstruction of the head and neck. Ann Plastic Surg. **52** (2), pp. 148–155; discussion 156–157, 2004.
45. Perktold K, Resch M, Peter RO: Three-dimensional numerical analysis of pulsatile flow and wall shear stress in the carotid artery bifurcation. J Biomech. **24** (6), pp. 409–420, 1991.
46. Steinman DA, Vinh B, Ethier CR, Ojha M, Cobbold RSC, Johnston KW: A numerical simulation of flow in a two-dimensional end-to-side anastomosis model. J Biomech Eng. **115** (1), pp. 112–118, 1993.
47. Steinman DA, Ethier CR: The effect of wall distensibility on flow in a two-dimensional end-to-side anastomosis. J Biomech Eng. **116** (3), pp. 294–301, 1994.
48. Perktold K, Leuprecht A, Prosi M, Berk T, Czerny M, Trubel W, Schima H: Fluid dynamics, wall mechanics, and oxygen transfer in peripheral bypass anastomoses. Ann Biomed Eng. **30** (4), pp. 447–460, 2002.
49. Roussis PC, Giannakopoulos AE, Charalambous HP: Suture Line Response of End-to-Side Anastomosis: A Stress Concentration Methodology. Cardiovasc Eng Technol. **6** (1), pp. 36–48, 2015.
50. Al-Sukhun J, Lindqvist C, Ashammakhi N, Penttilä H: Microvascular stress analysis. Part I: simulation of microvascular anastomoses using finite element analysis. Br J Oral Maxillofacial Surg. **45** (2), pp. 130–137, 2007.
51. Al-Sukhun J, Penttilä H, Ashammakhi N: Microvascular stress analysis: Part II. Effects of vascular wall compliance on blood flow at the graft/recipient vessel junction. J Craniofacial Surg. **22** (3), pp. 883–887, 2011.
52. Liu Y, Wang S, Hu SJ, Qiu W: Mechanical analysis of end-to-end silk-sutured anastomosis for robot-assisted surgery. Int J Med Robotics + Comput Assisted Surg: MRCAS **5** (4), pp. 444–451, 2009.
53. Li H, Agarwal J, Coats B, Gale BK: Optimization and evaluation of a vascular coupling device for end-to-end anastomosis: A finite-element analysis. J Med Devices. Transactions of the ASME 10 (1), 011003, 2016.
54. Zienkiewicz OC, Taylor RL, Zhu JZ: The Finite Element Method: Its Basis and Fundamentals, 6th Edition, Butterworth-Heinemann, 2005.

55. Zienkiewicz OC, Watson M, King IP: A numerical method of visco-elastic stress analysis. Int J Mech Sci. **10** (10), pp. 807–827, 1968.
56. Ahmad S, Irons BM, Zienkiewicz OC: Analysis of thick and thin shell structures by curved finite elements. Int J Numerical Methods Eng. **2**, pp. 419–451, 1970.
57. Timoshenko S, Woinowsky-Krieger S: Theory of plates and shells, 2nd Edition, New York: McGraw-Hill, 1959.
58. Sokolnikoff IS: Mathematical theory of elasticity, 2nd Edition, McGraw-Hill, 1946.
59. Courant R: Variational methods for the solution of problems of equilibrium and vibrations. Bull Am Math Soc. **49** (1), pp 1–23, 1943.
60. Rickard RF, Meyer C, Hudson DA: Computational modeling of microarterial anastomoses with size discrepancy (small-to-large). J Surg Res. **153** (1), pp. 1–11, 2009.
61. Karanasiou GS, Gatsios DA, Lykissas MG, Stefanou KA, Rigas GA, Lagaris IE, Kostas-Agnantis IP, Gkiatas I, Beris AE, Fotiadis DI: Modeling of blood flow through sutured micro-vascular anastomoses, in: Engineering in Medicine and Biology Society, 2015 37th Annual International Conference of the IEEE, 2015, pp. 1877–1880.
62. Burton AC: Physiology and biophysics of the circulation: an introductory text, Year Book Medical Publishers, 1972.
63. Abbott W, Bouchier-Hayes D: The role of mechanical properties in graft design, Graft materials in vascular surgery 59.
64. Kahveci K, Becker BR: A numerical model of pulsatile blood flow in compliant arteries of a truncated vascular system. International Communications in Heat and Mass Transfer. **67** (Supplement C), pp. 51–58, 2015.
65. Chandran K, Gao D, Han G, Baraniewski H, Corson J: Finite-element analysis of arterial anastomoses with vein, dacron and ptfe graffs. Med Biol Eng Comput. **30** (4), pp. 413–418, 1992.
66. Deng X, Guidoin R: Arteries, veins and lymphatic vessels, in: J. Black, G. Hastings (Eds.), Handbook of Biomaterial Properties, Springer, 1998, pp. 81–105.
67. Patel DJ, Janicki JS, Carew TE: Static Anisotropic Elastic Properties of the Aorta in Living Dogs. Circulation Res. **25** (6), pp. 765–779, 1969.
68. Skacel P, Bursa J: Poisson's ratio of arterial wall - Inconsistency of constitutive models with experimental data. J Mech Behav Biomed Mater. **54**, pp. 316–327, 2016.
69. ANSYS, Structural 18.2: ANSYS, Inc. academic research, Commercial software (January 2017).
70. ANSYS, Introduction to ANSYS CFX 16.0 - Lecture 4: Domains, Boundary Conditions and Sources, Tech. rep., ANSYS, Inc. (2015). URL https://support.ansys.com
71. Vignon-Clementel IE, Figueroa CA, Jansen KE, Taylor CA: Outflow boundary conditions for threedimensional finite element modeling of blood flow and pressure in arteries. Comput Meth Appl Mech Eng. **195** (29–32), pp. 3776–3796, 2006.
72. Crelle AL: Démonstration nouvelle du théorème du binôme. Journal für die reine und angewandte Mathematik. **4**, pp. 305–308, 1829.
73. Cheng AHD, Cheng DT: Heritage and early history of the boundary element method. Eng Anal Boundary Elements. **29** (3), pp. 268–302, 2005.
74. James I: Remarkable mathematicians, Cambridge University Press, 2009.
75. Ugural AC, Fenster SK: Advanced strength and applied elasticity, 4th Edition, Prentice Hall, 2003.
76. Rao SS: Mechanical vibrations, 5th Edition, Pearson, 2010.
77. Zhu Z, Wang X, Huang J, Li J, Ding X, Wu H, Yuan Y, Song X, Wu Y: Mechanical versus Hand-Sewn Venous Anastomoses in Free Flap Reconstruction: A Systematic Review and Meta-Analysis. Plastic and Reconstructive Surg. **141** (5), p. 1272, 2018.
78. Abramowitz M, Stegun IA: With formulas, graphs, and mathematical tables. National Bureau of Standards Applied Mathematics Series. **e 55**, p. 953, 1965.
79. ASME - Boiler and Pressure Vessel Code Complete Set (2017). URL https://www.asme.org
80. de Carvalho MVH, Marchi E, Lourenço EA: Comparison of Arterial Repair through the Suture, Suture with Fibrin or Cyanoacrylate Adhesive in Ex-Vivo Porcine Aortic Segment. Brazilian J Cardiovasc Surg. **32** (6), pp. 487–491, 2017.